Hindawi
Nanomaterials and Nanotechnology
Volume 2023, Article ID 9793804, 17 pages
https://doi.org/10.1155/2023/9793804

Research Article

Synthesis, Characterization, and Environmental Applications of Cu-Ni-Doped Bismuth Molybdate

Kashaf Sehar,[1] Muhammad Saeed,[2] Maida Murtaza,[1] Manzar Zahra,[3] and Amir Waseem[1]

[1]*Department of Chemistry, Quaid-i-Azam University, Islamabad 45320, Pakistan*
[2]*School of Chemistry, University of the Punjab, Lahore 54590, Pakistan*
[3]*Department of Chemistry, Lahore Garrison University, Lahore, Pakistan*

Correspondence should be addressed to Amir Waseem; amir@qau.edu.pk

Received 8 August 2022; Accepted 23 December 2022; Published 9 August 2023

Academic Editor: Raphael Schneider

Bismuthoxide-based catalysts gained attention for photocatalytic remediation of environmental pollutants owing to their low cost, feasibility, stability, small, and tunable band gap. In the present work, bismuth molybdate was modified via transition metal doping to achieve maximum catalytic efficiency. This aim was accomplished by synthesizing novel Cu^{2+} and Ni^{2+} codoped bismuth molybdate ($CuNi/Bi_2MoO_6$, Cu/Bi_2MoO_6, and Ni/Bi_2MoO_6) which were utilized for heavy metal reduction and dyes degradation. Pure bismuth molybdate was also fabricated for comparative studies. All the prepared samples were characterized by XRD, Raman spectroscopy, SEM, and EDX. Optical studies for band gap calculations were carried out by UV-Visible spectrophotometry and decrease in band gap was observed in doped materials. Pseudo-first-order kinetic studies were performed to find the rate constants and regression values for Cr(VI) reduction and degradation of rhodamine B and malachite green using $CuNi/Bi_2MoO_6$. Codoped bismuth molybdate exhibited more than 95% photocatalytic performance for Cr(VI) reduction and degradation of rhodamine B and malachite green dyes. Reusability of catalyst was confirmed up to six cycles. Considering its catalytic proficiency, $CuNi/Bi_2MoO_6$ is anticipated to be utilized for more environment friendly applications in future.

1. Introduction

Generally, traditional methodologies of water treatment include biological method (such as aerobic and anaerobic treatments), physical processes, or chemical treatments. These methods have been broadly utilized in the treatment of industrial effluents, but still there are some demerits associated with these techniques [1]. Biological methods are remarkable due to their low cost and accessibility, but they are incapable to degrade synthetic dyes because generally they are not vulnerable for aerobic biodegradation. Physical methods (such as filtration, coagulation/flocculation, and adsorption) are normally helpful, but they face the drawback of post treatment of solids and coagulated waste with functioning cost. Chemical treatments also suffer disadvantages, because toxic and carcinogenic substances are formed as by products; they require high dosage of chemicals, less effectiveness, and incomplete mineralization. Since all methods have some disadvantages, the establishment of better method for the treatment of wastewater is of prime significance for longer term ecological practicality of textile industry [2].

Advanced oxidation processes (AOPs), also known as oxidative degradation processes, involve the generation of highly reactive hydroxyl radicals ($OH^{\bullet}$), hydrogen peroxide (H_2O_2), and superoxide anionic radicals ($O_2^{\bullet-}$) in adequate quantity to improve water purification process. AOPs are basically used for the degradation of organic and inorganic contaminants present in water and wastewater [3]. During AOPs, these radicals acting as efficient oxidizing agents, satisfactorily degrade the pollutants and convert wastewater toxins into minimal and even nontoxic substances.

Photocatalysis refers to the acceleration of a photoreaction involving a catalyst. Among various advanced oxidation processes, semiconductor mediated photocatalysis have proven to be specifically remarkable in current era because of

their high capability for mineralization of organic pollutants present in the environment [4, 5]. Bismuth based compounds such as Bi_2O_3, Bi_2WO_6, $BiVO_4$, Bi_2MoO_6, BiOX (X = Cl, Br, I), and $Bi_{12}GeO_{20}$ have been emerged as visible light driven photocatalysts associated with high oxidation performance and charge mobility which results excellent photocatalytic performance. Amongst these Bismuth compounds, Bi_2MoO_6 has expressed extraordinary properties such as gas sensitivity, ion conductivity, luminescence, dielectric nature, and photocatalytic properties [6].

Bi_2MoO_6 is found to possess a unique aurivillus structure constructing alternating $(Bi_2O_2)^{2+}$ layers and $(MoO_4)^{2-}$ perovskite slabs. Both bismuth oxide layer with Bi-O structure and a perovskite with corner shared octahedral Mo-O structure promote efficient electron conductivity, which is responsible for its excellent dielectric behavior, ion conductive nature, luminescence, and catalytic features [7]. Bismuth molybdate possesses some more interesting properties like resistivity towards corrosion, mesoporosity, less cost, brilliant chemical stability, and distinguished physiochemical properties, which has also great contribution to its better photocatalytic efficiency [8]. Bi_2MoO_6 is n-type semiconductor (majority of charge carriers are electrons) having up shifted valance band, it has a narrow band gap, i.e., 2.5–2.8 eV, which makes it an amazing catalyst [9]. It has capability to engage more sunlight; the smaller band gap is due to the hybridization between Bi 6s and O 2p orbitals.

Bismuth molybdate is a leading photocatalyst among other pure semiconductor photocatalysts due to its narrow band gap, but still certain limitations are associated with pure BMO. Practical applications of BMO are challenging owing to its fast electron hole recombination, slow carrier migration, and poor surface chemical states [10]. Poor quantum yield and low visible light efficiency are also the obstacles to high photocatalytic efficiency of BMO [11]. So, it is mandatory to prospect some modification methods such as Z-scheme, doping, heterostructures, nanocomposites, or dye sensitization to overcome these issues. Doping of various suitable metals is a powerful method to enhance photo induced functioning in wide wavelength range, redesigning band gap, diminishing photogenerated electrons/holes pairs recombination, and upgrading the gross efficiency of photocatalyst [12]. Because of distinct spectral characteristics and d orbital configuration, transition metal doping is very fruitful technique to extend the absorption from ultraviolet to visible region. It may modify the VB or CB or may add a new band into the preliminary band gap [13]. So, in this research work, we modified Bi_2MoO_6 by doping with Cu^{2+} and Ni^{2+} metal ions.

We synthesized pure and modified Bi_2MoO_6 by hydrothermal method to achieve anisotropic crystals growth, high purity, and fine particles under controlled conditions [14]. Prepared samples were characterized by XRD, SEM, EDX, and Raman spectroscopy, and optical studies and effect of codoping on photocatalytic efficiency was examined by photoreduction of hexavalent chromium and photodegradation of rhodamine B (RhB) and malachite green (MG) by UV-Vis photo spectrometry. In-depth research was also carried out on the prospective photocatalytic mechanism and the factors driving it.

2. Experimental Methods

2.1. Materials. All chemicals and reagents were purchased from Sigma Aldrich, Fluka, and E. Merck. Bismuth nitrate pentahydrate ($Bi(NO_3)_3{\cdot}5H_2O$), nitric acid (HNO_3), ammonium molybdate tetrahydrate ($(NH_4)_6Mo_7O_{24}{\cdot}4H_2O$), sodium hydroxide (NaOH), ethanol, and deionized water were used in the synthesis of bismuth molybdate. Nickel nitrate hexahydrate ($Ni(NO_3)_2.6H_2O$) and copper nitrate hexahydrate ($Cu(NO_3)_2.6H_2O$) were used as doping source. All the analytical grade chemicals were utilized without any further purification.

2.2. Synthesis of Cu^{+2} and Ni^{+2} Codoped Bi_2MoO_6. Bismuth molybdate nanoparticles were synthesized by facile hydrothermal method [15], as previously reported. Initially, three solutions were made labelled as solution A, solution B, and solution C. Solution A was formed by dissolving 0.01 moles of $Bi(NO_3)_3{\cdot}5H_2O$ in 50 mL of 3M nitric acid. Solution B was obtained by dissolving 7.1 mmol of $(NH_4)_6Mo_7O_{24}{\cdot}4H_2O$ in 50 mL of 2M sodium hydroxide. Solution A was dropwise added to solution B under continuous magnetic stirring, thus forming solution C. 3% (weight percentage) of each dopant, i.e., $Cu(NO_3)_2{\cdot}6H_2O$ and $Ni(NO_3)_2{\cdot}6H_2O$ was dissolved in solution C and pH of this solution was adjusted to 7 by adding required amount of 2M NaOH solution. After 30 minutes stirring, this catalyst precursor was poured into the autoclave teflon lining and set of hydrothermal treatment for 16 hours at 160°C. Autoclave was allowed to auto cool to room temperature and brownish yellow precipitates of bismuth molybdate were obtained which were separated by vacuum filteration and washed multiple times with distilled water and ethanol. Finally, the product was dried at 80°C for 12 hours. For reference, pure Bi_2MoO_6, 6% Cu^{+2}-doped Bi_2MoO_6 and 6% Ni^{+2}-doped Bi_2MoO_6 were also synthesized by same procedure.

2.3. Characterization. PXRD spectra of pure and modified bismuth molybdate were achieved by a powder diffractometer (Model X'Pert powder X-ray diffractometer from PANalytical, Holland). Nickel filtered Cu Kα radiations were used to get XRD patterns and the scan rate of 2° in 2θ/min was maintained at diffraction angle of 2θ = 5–80°C. Data were recorded at 30 mA emission current, 40 kV accelerating voltage, 0.025 step size, 0.4 sec step time, and 0.06/sec scan speed. SEM images were collected by VEGA3 TESCAN field emission electron microscope to determine the size and morphology of materials. Resolution was kept 500 nm and accelerating voltage was kept 10.00 kV while taking the images. Elemental analysis was performed by Energy Dispersive X-Ray Detector (EDS, Thermo Noran VANTAG-ESI). Raman measurements were carried out at room temperature using Raman Spectrometer (BWTEK MiniRam BTR-111 Miniature) with the Raman shift ranging from 200 cm^{-1} to 1500 cm^{-1}. Argon ion laser was employed as

a mean of excitation (514 nm). Optical studies for band gap estimation were carried out by using spectrophotomter (Model UV-1700 Shimadzu) in the range of 200 to 800 nm, water was used as solvent.

2.4. Photocatalytic Studies. Photocatalytic performance of prepared materials was examined for the degradation of MG, RhB, and photoreduction of Cr(VI) under 100 watt LED light with output of 40 k Lux. In a standard analysis, a suitable amount of photocatalyst was dispersed in 40 mL aqueous solution of different concentrations of RhB, MG dyes, and $K_2Cr_2O_7$ (with 1 mL formic acid added). The solutions were thoroughly stirred using magnetic stirrer (Model VELP Scientifica) at normal temperature under visible light source. 3 mL of suspension was taken at specific time intervals and centrifuged to eliminate the catalyst. The concentration of dye residual in the clear solution was evaluated by UV-Visible spectrophotometer with respect to lambda max. of RhB, MG, and Cr(VI) at 555 nm, 617 nm, and 372 nm, respectively. To assess the photocatalytic activity of the as prepared catalyst CuNi/BMO for colourless organic pollutants, bisphenol A was used before using with intensely coloured dyes (supplementary data (available here)).

Photo degradation efficiency and photoreduction efficiencies were calculated by the following formula:

$$\text{Percentage degradation efficiency } (\%) = \frac{(C_o - C_t)}{C_o} \times 100, \quad (1)$$

where C_o = initial concentration of dye and C_t = dye concentration after irradiation time, t.

The Langmuir–Hinshelwood model was used in the determination of reaction kinetics. The following equation was used for the determination of rate constant and R^2 values:

$$ln\left(\frac{C_t}{C_0}\right) = -k_{app}\, t, \quad (2)$$

"kapp" signifies the rate constant for pseudo-first-order reduction reaction and "t" is the time required for the completion of the reaction. Rate constant was measured from the slope of the graph plotted between ln (C_t/C_0) on the y-axis and t on the x-axis.

3. Results and Discussion

3.1. X-Ray Diffraction. XRD patterns of fabricated materials are shown in Figure 1. The orthorhombic geometry of Bi_2MoO_6 is represented by sharp peaks in the diffraction pattern at 28.11°, 32.98°, 46.96°, and 56.11°, which are related to (131), (200), (062), and (331) crystallographic planes, respectively. These results are consistent with JCPDS card number 01-072-1524 and previous reports [16]. No diffraction peak appeared due to transition metal ions or any other impurity which confirms that same geometry is present in all the samples, and it also indicates that all the dopant may have entered into the lattice.

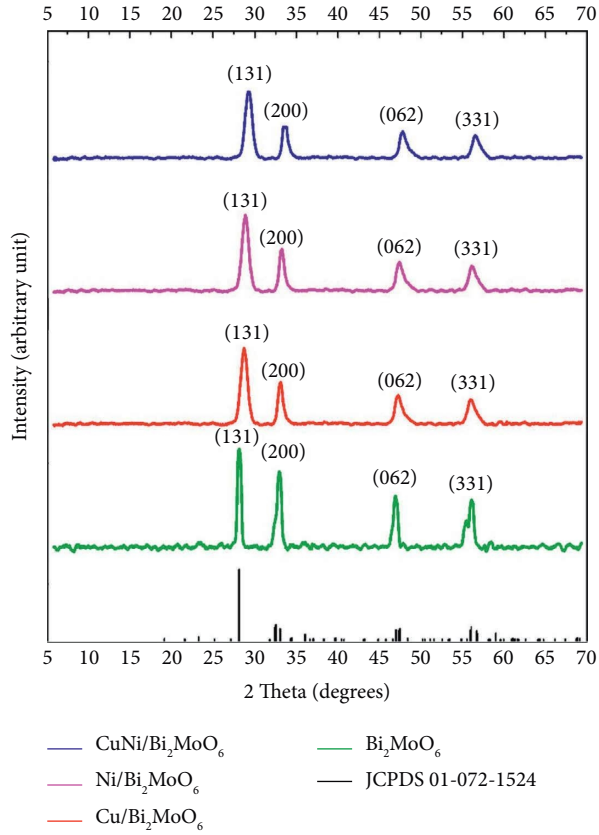

Figure 1: XRD patterns of BMO, Cu/BMO, Ni/BMO, and Cu-Ni/BMO.

On doping, all the peaks in diffraction pattern shifted towards higher angle value of 2θ as compared to pure BMO, which can be justified due to difference in ionic radius of Bi^{3+} (103 pm) and the dopant metal ion Cu^{2+} (73 pm) and Ni^{2+} (70 pm). Lattice parameters and respective cell volumes of all the prepared samples are given in Table 1. There is decrease in lattice parameters and cell volumes of Cu/Bi_2MoO_6, Ni/Bi_2MoO_6, and Cu-Ni/Bi_2MoO_6 as compared to pure Bi_2MoO_6, which possibly due to the transition metal ions have substituted Bi^{3+} in Bi_2MoO_6 lattice. Peak broadening and decrease in intensity in diffraction patterns of doped materials is a possible indication of doping with smaller atoms.

The crystallite size was calculated using the Scherrer equation:

$$D = \frac{K.\lambda}{(\beta \cos\theta)}, \quad (3)$$

where D = diameter of crystallite, K = shape factor having value 0.9, λ = wavelength of incident X-ray having value 1.542 Å, β = full-width hall maxima of corresponding diffraction peak, and θ = bragg's angle (in radians).

3.2. Raman Spectroscopy. Raman spectra of pure Bi_2MoO_6, Cu/Bi_2MoO_6, Ni/Bi_2MoO_6, and Cu-Ni/Bi_2MoO_6 are given in Figure 2. Six vibration bands are noticed at 845 cm^{-1},

Table 1: Cell parameters, cell volume, and crystallite size of materials.

Materials	Lattice parameters			Cell volume (Å)^3	d-spacing (Å)	Crystallite size (nm)
	a (Å)	b (Å)	c (Å)			
Bi_2MoO_6	5.506	16.226	5.4870	490.21	2.379	27.03
Cu/Bi_2MoO_6	5.504	16.221	5.482	489.43	2.118	24.98
Ni/Bi_2MoO_6	5.501	16.201	5.470	487.46	1.934	24.10
$Cu\text{-}Ni/Bi_2MoO_6$	5.493	16.175	5.468	485.82	1.6246	23.47

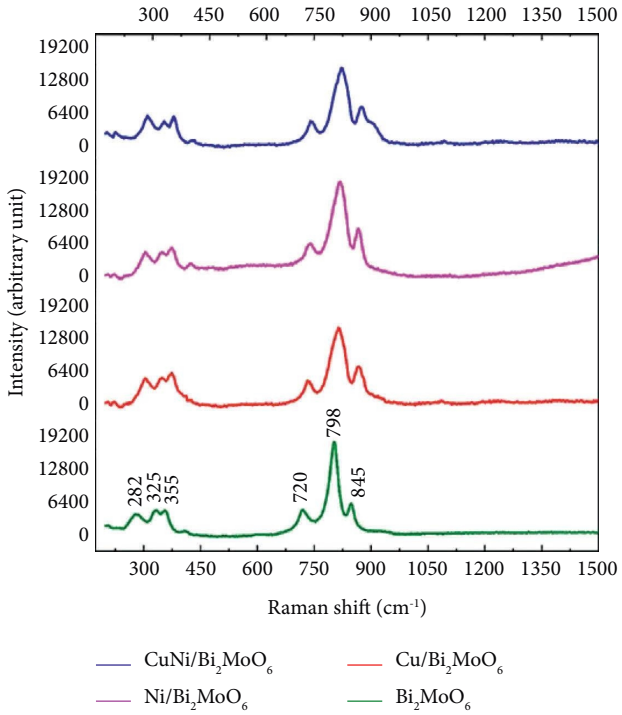

Figure 2: Raman spectra of BMO, Cu/BMO, Ni/BMO, and Cu-Ni/BMO.

798 cm^{-1}, 720 cm^{-1}, 355 cm^{-1}, 325 cm^{-1}, and 282 cm^{-1} in the spectrum of BMO. The symmetric stretch of MoO6 octahedron generates A_{1g} peak at 798 cm^{-1} [17]. Two shoulder peaks at around 845 cm^{-1} (corresponding to A_{2u} mode) and 720 cm^{-1} (corresponding to E_u mode) are associated with asymmetric stretches of Mo-O [18]. The peaks which are present below 400 cm^{-1}, are ascribed to stretching vibrations of Bi-O and lattice modes [17]. The results are compatible with prior reported work on BMO. All peaks were observed in modified samples with slight shifts which indicate that transition metal doping might have resulted in some tiny structural changes in bismuth molybdate. Anyhow, all the samples possess same orthorhombic phase [19]. No considerable change in intensity is observed in the band related to MoO_6 octahedron while there is an increase in intensity in the peaks below 400 cm^{-1} which are attributed to Bi-O. These observations are logical to make us believe that dopant has interacted with Bi^{3+} in the lattice instead of Mo^{6+}.

3.3. Scanning Electron Microscopy. SEM images of pristine Bi_2MoO_6 and $Cu\text{-}Ni/Bi_2MoO_6$ were obtained for the comparison of surface morphologies as shown in Figures 3(a)–3(d) at different resolutions. It can be seen that BMO is made up of irregular shaped and globular nanoparticles but Cu-Ni/BMO has flowerlike microspheres which are aggregated by nanosheets [20]. Modified BMO exhibited fluffy appearance attributed to surface roughness, which may be responsible for increased contact area resulting in enhanced photocatalytic activity.

3.4. Energy-Dispersive X-Ray Spectroscopy. Figures 4(a) and 4(b) demonstrate the elemental composition study of pure BMO and codoped BMO particles from the EDX plot of respective SEM images. Bi_2MoO_6 is confirmed by high peaks of Bi, Mo, and O as base material. Moreover, EDX spectra also show that the loading of Cu (3%) and Ni (3%) is present in modified BMO.

3.5. Optical Study and Band Gap Estimation. In semiconductor nanomaterials, valance band electrons migrate to the conduction band after absorbing the sufficient amount of energy. The relation between absorption spectra and band gap energy is expressed by the Tauc equation, written as follows [21]:

$$(\alpha h\upsilon) = k(h\upsilon - \mathrm{Eg})^n, \tag{4}$$

where $h\upsilon$ = energy of photon, n = type of transition ($n = 1/2$ for direct transition and $n = 2$ for indirect transition), k = tailing parameter (independent of energy), Eg = energy of band gap [22], and α = coefficient of absorption (calculated from Beer–Lambert law.)

Extrapolation of linear region of plot ($\alpha h\upsilon$) [2] vs. energy ($h\upsilon$) gives the value of optical band gap, Eg in UV-Vis wavelength range (200–800 nm). Difference in the values of band gap can be due to various reasons like dimensions of grains, transition type (direct or indirect), annealing treatment, and doping [23]. The accessibility of oxygen vacancies can also create new state between valance band and conduction band resulting in the narrowing of band gap. Figure 5(a) gives the Tauc plot of pure Bi_2MoO_6 which shows the value of Eg around 2.83 eV which corresponds to the previously reported work [9]. Figure 5(b) shows the band gap of the Cu-doped Bi_2MoO_6 catalyst. Tuning of band gap was observed after the incorporation of copper into the

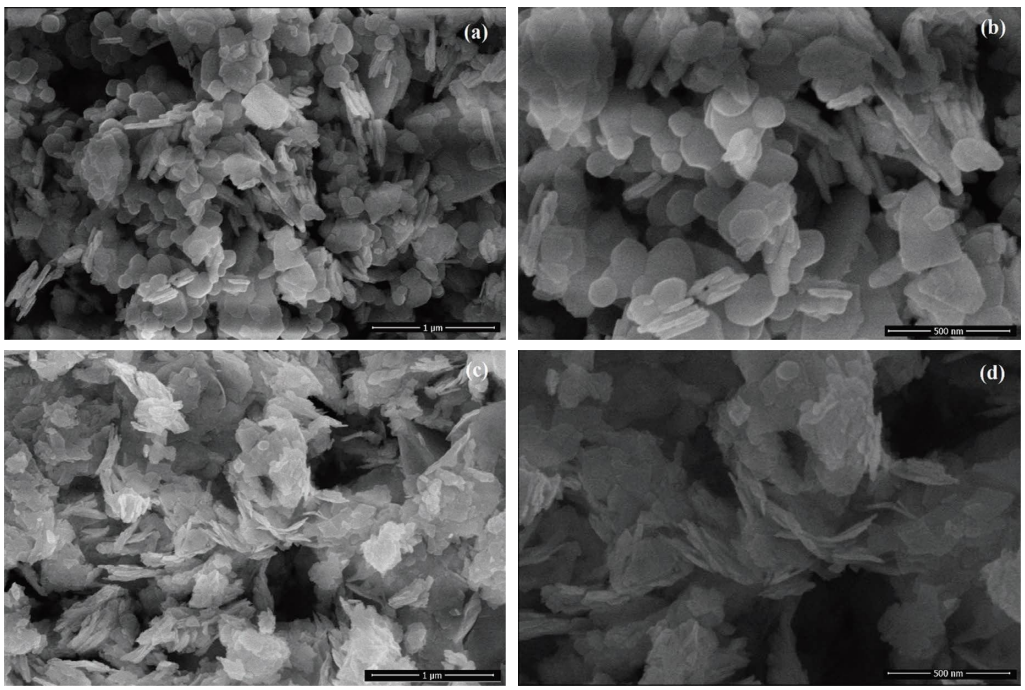

Figure 3: SEM images of (a, b) pure BMO and (c, d) CuNi/BMO.

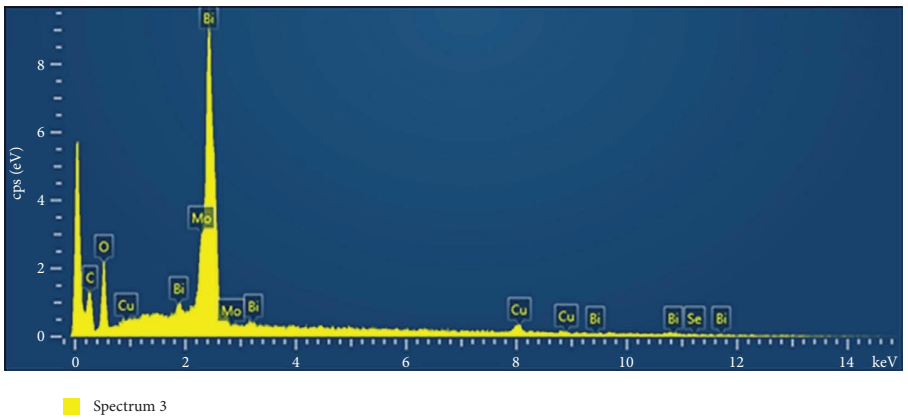

(a)

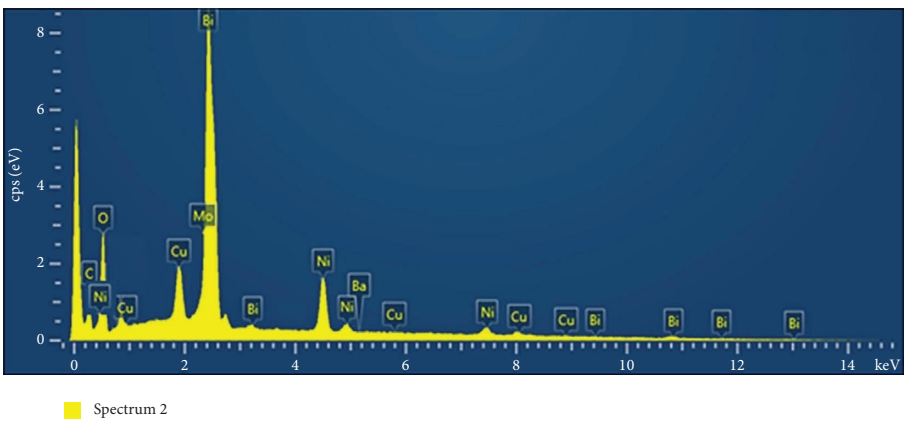

(b)

Figure 4: EDX spectrum of (a) pure BMO and (b) CuNi/BMO.

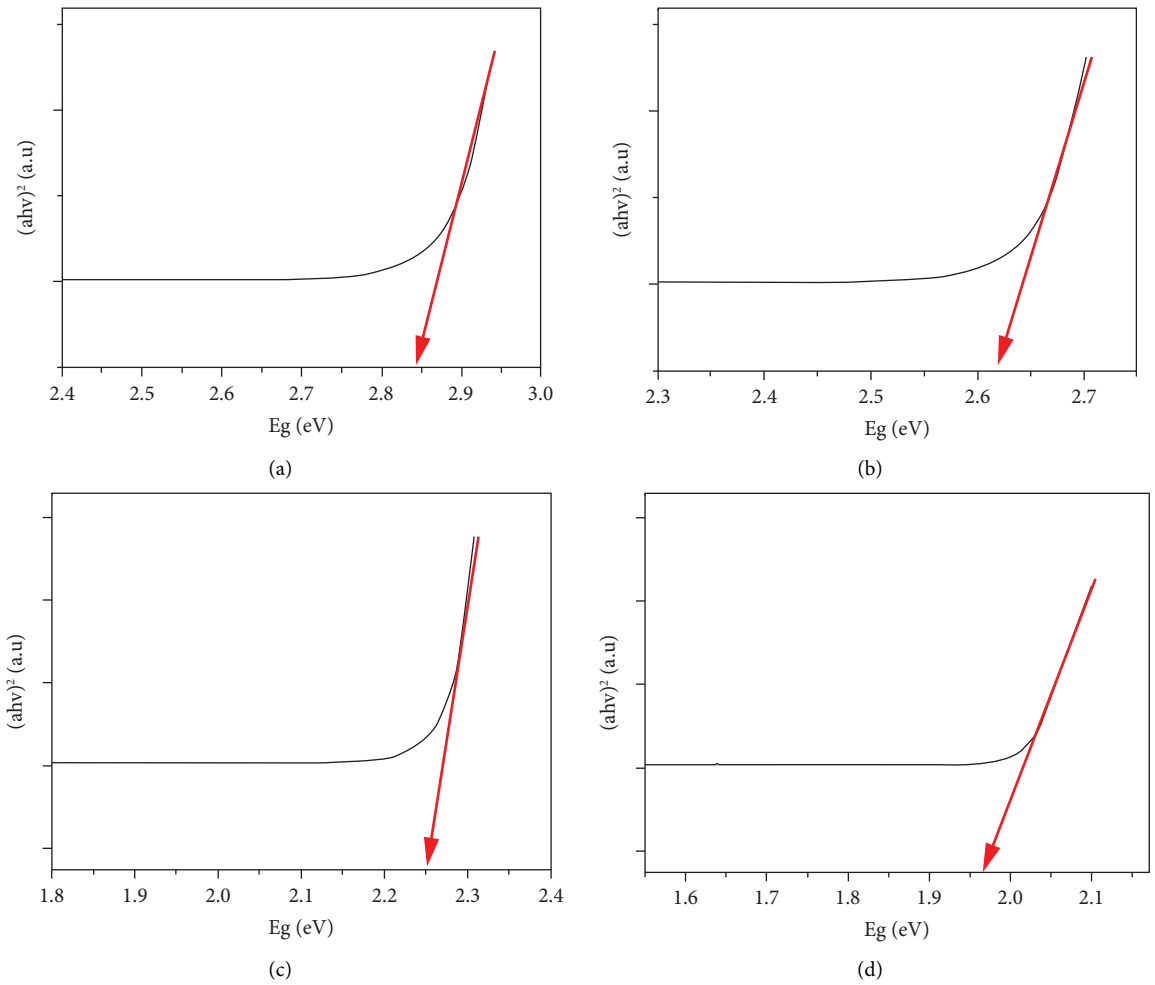

Figure 5: Tauc plot of BMO: (a) Bi_2MoO_6, (b) Cu/Bi_2MoO_6, (c) Ni/Bi_2MoO_6, and (d) $CuNi/Bi_2MoO_6$.

lattice, which was found to be 2.61 eV. Similarly, the band gap of Ni-doped Bi_2MoO_6 was observed at 2.24 eV in Tauc plot, shown in Figure 5(c). It was noticed that copper and nickel codoped Bi_2MoO_6 showed minimum value of band gap among all the samples. Tauc plot of $CuNi/Bi_2MoO_6$ is given in Figure 5(d), which gives the value of Eg at 1.97 eV.

3.6. Photoreduction Studies of Hexavalent Chromium. Photocatalytic ability of CuNi/BMO for the reduction of hexavalent chromium to trivalent chromium was determined by UV-Vis spectrophotometry, and it was proved to be an excellent reducing agent. Aqueous solution of potassium dichromate was used as a source of Cr(VI). Hole scavengers are generally used for efficient reduction of heavy metals; in this work, formic acid was employed as the hole scavenger. Role of formic acid on reduction of hexavalent chromium was confirmed through various ways; firstly, formic acid was used solely as reducing agent but there was no significant reduction even after 24 hours as shown in Figure 6. It indicates that formic acid is incapable to reduce

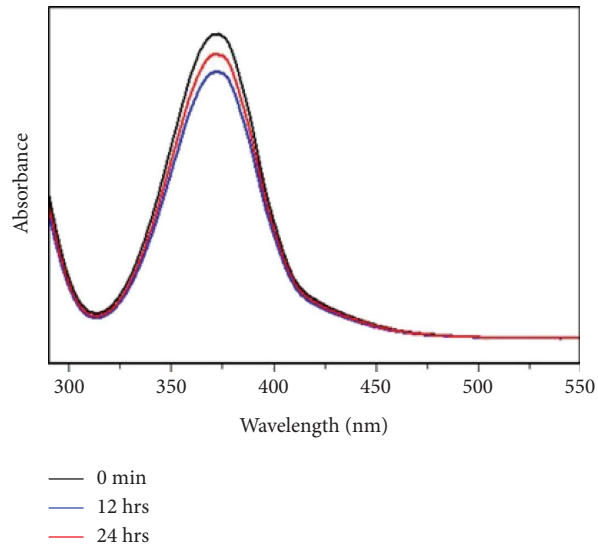

Figure 6: Effect of formic acid on Cr(VI) reduction in the absence of a catalyst.

Cr(VI) completely in the absence of catalyst. Similarly, Cr(VI) reduction using CuNi/BMO was examined with and without formic acid as shown in Figures 7(a) and 7(b). It was concluded that CuNi/BMO did not completely reduce the hexavalent chromium while its performance incredibly enhanced when formic acid was also added to reaction solution.

3.6.1. Mechanism of Cr(VI) Reduction. Electrons occupying the conduction band are responsible for the reduction of heavy metals. For photoreduction process, the reduction potential of conduction band must be smaller (less positive) positive than that of heavy metal, so that the electrons can flow from conduction band of catalyst to the metal to reduce it according to energy flow. This condition is fulfilled by bismuth molybdate catalyst, its reduction potentials of conduction band and valance band are −0.33 eV and 2.43 eV [24], respectively, while that of $Cr_2O_7^{2-}$/Cr (III) is 1.38 V [25].

$$\begin{aligned} \mathbf{BMO} + \mathbf{h}\upsilon &\longrightarrow \mathbf{BMO}\,(\mathbf{e}^-\ (\mathbf{CB}) + \mathbf{h} + (\mathbf{VB})) \\ \mathbf{H_2O} + \mathbf{h}^+ &\longrightarrow \bullet\mathbf{OH} + \mathbf{H}^+ \end{aligned} \tag{5}$$

$$\mathbf{Cr_2O_7}^{2^-} + \mathbf{14H}^+ + \mathbf{6e}^- \rightarrow \mathbf{2Cr}^{3+} + 7\mathrm{H_2O} \quad \left(\mathrm{E}^0 = 1.38\mathrm{V}\right) \tag{6}$$

Formic acid undergoes sacrificial oxidation and speeds up the reaction by removing holes from the system, because reduction is mainly carried out by electrons. It decreases the electron hole pair recombination as well. Formic acid takes part in the reduction mechanism according to following equations:

$$\begin{aligned} \mathbf{HCOO}^- + \bullet\mathbf{OH} &\rightarrow \bullet\mathbf{CO_{2-}} + \mathbf{H_2O} \\ \mathbf{Cr_2O_7}^{2^-} + \bullet\mathbf{CO_{2^-}} + \mathbf{14H}^+ + &\rightarrow \mathbf{2Cr}^{3+} + \mathbf{CO_2} + \mathbf{7H_2O} \end{aligned} \tag{7}$$

3.6.2. Selection of Appropriate Catalyst for Cr(VI) Reduction. Using UV-Visible absorption spectrophotometry, the photocatalytic performance BMO, Cu/BMO, Ni/BMO, and CuNi/BMO for the reduction of hexavalent chromium to trivalent chromium was examined by taking 0.03 g of catalyst, 1 mL of formic acid, and 10 ppm of potassium dichromate solution. The resulting solutions were irradiated under visible light for one hour and continuous magnetic stirring. The most efficient of these catalysts was selected owing to its effectiveness towards the photoreduction. From UV absorption data, it was noticed that the Cr(VI) peak at 372 nm entirely disappeared and new peak of Cr (III) at (350 nm) start originating. These results showed that CuNi/BMO photocatalyst exhibited the highest photocatalytic efficiency among all the four photocatalyst as shown in Figure 8(a).

3.6.3. Effect of pH on Cr(VI) Reduction. Hexavalent chromium photoreduction was optimised to ensure maximum CuNi/Bi_2MoO_6 catalytic efficiency by examining the effects of multiple factors, with pH being one of the main factors affecting the reduction process. pH of solution was modulated with 1M NaOH and 1M HCL at the start of the reaction and its effect on photoreduction was examined in pH range 2–10, initial concentration of potassium dichromate solution 10 ppm (40 mL) and catalyst dose of 0.02 g for 30 minutes. Photoreduction efficiency was found to be maximum at pH 2 as shown in Figure 8(b). Existence of Cr^{6+} is highly pH dependant, in acidic media (pH < 6), $HCrO_4^-$ is present in equilibrium with $Cr_2O_7^{2-}$, which can be easily reduced owing to high reduction potential of $Cr_2O_7^{2-}$ as shown in equation (6). Decline in photoreduction efficiency at higher pH values may be due to the production of CrO_4^{2-} which is less reducible due to its lower reduction potential (as shown in equation (8)) resulting in lower degree of photoreduction.

$$\mathbf{CrO_4}^{2^-} + \mathbf{H_2O} + \mathbf{3e}^- \rightarrow \mathbf{Cr\,(OH)_3} + \mathbf{5OH}^- \quad \left(\mathrm{E}^0 = 0.13\mathrm{V}\right) \tag{8}$$

Moreover, Cr (III) form precipitates of Cr $(OH)_3$ in basic media which hinder the light penetration into reaction solution, consequently, photoreduction efficiency decreases [26].

In addition, as isoelectric point of BMO is 5.4 [27] so its surface will be positively charged at pH < 6 and there will be negative charges on surface at pH > 6. This is also a major reason of better efficiency at pH = 2 because electrostatic forces of attraction will be developed between catalyst and negatively charged potassium dichromate ions leading to highest efficiency. As there is no considerable difference in reduction efficiency at pH 2 and pH 4, so pH 4 was selected as optimum pH because catalyst poisoning may occur at harsh conditions.

3.6.4. Effect of Irradiation Time on Cr(VI) Reduction. Effect of irradiation time on photoreduction of Cr(VI) was analyzed by varying the time from 5 to 60 minutes by using 40 mL of 10 ppm $K_2Cr_2O_7$ solution with 0.02 g catalyst dose at pH 4. Effect of irradiation time is shown in Figure 8(c) which indicates that photoreduction efficiency of catalyst increases with the passage of time due to increase in electron transfer rate and becomes highest at 40 minutes. Hence, 40 minutes was selected as optimum time for further catalytic investigates.

3.6.5. Effect of Catalyst Dose on Cr(VI) Reduction. Catalyst dose is also an important factor in photocatalytic studies; its effect was studied under above-mentioned conditions by providing catalyst dose from 0.01 g to 0.05 g. Photocatalytic reduction efficiency of CuNi/BMO for Cr(VI) was increased by increasing catalyst dose upto 0.03 g as shown in Figure 9(d). This increased efficiency can be due to the formation of more active radicals with an increase in catalyst dose, which are mainly responsible for removal of contaminants. Further increasing the catalyst dose above 0.03 g led to the decline in efficiency, this is possibly due to the reason that surfeit catalyst particles can create

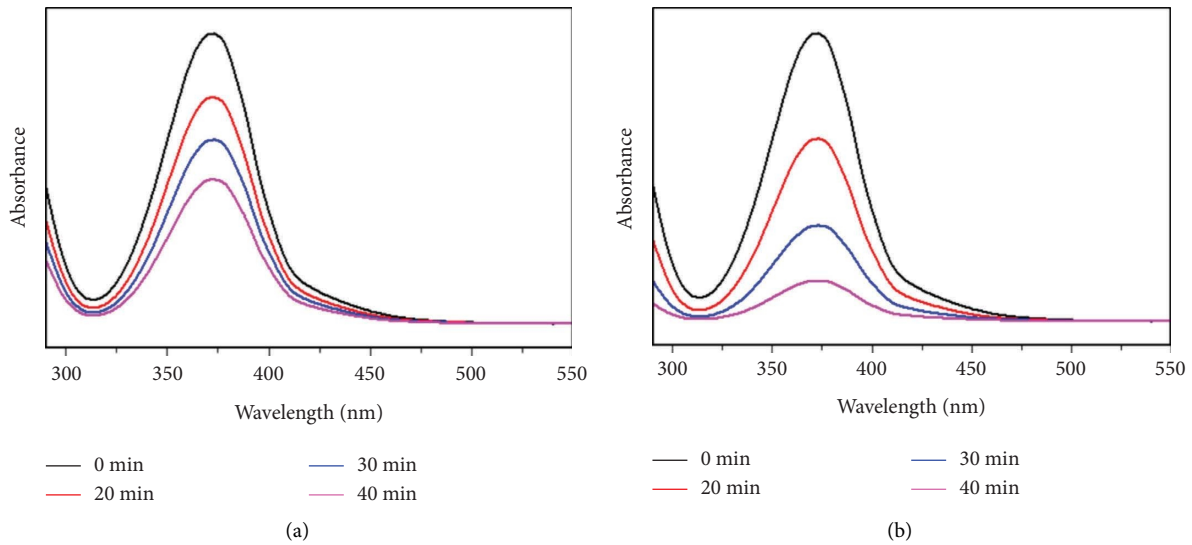

Figure 7: Photoreduction of Cr(VI) (a) by CuNi/BMO and (b) by CuNi/BMO + formic acid.

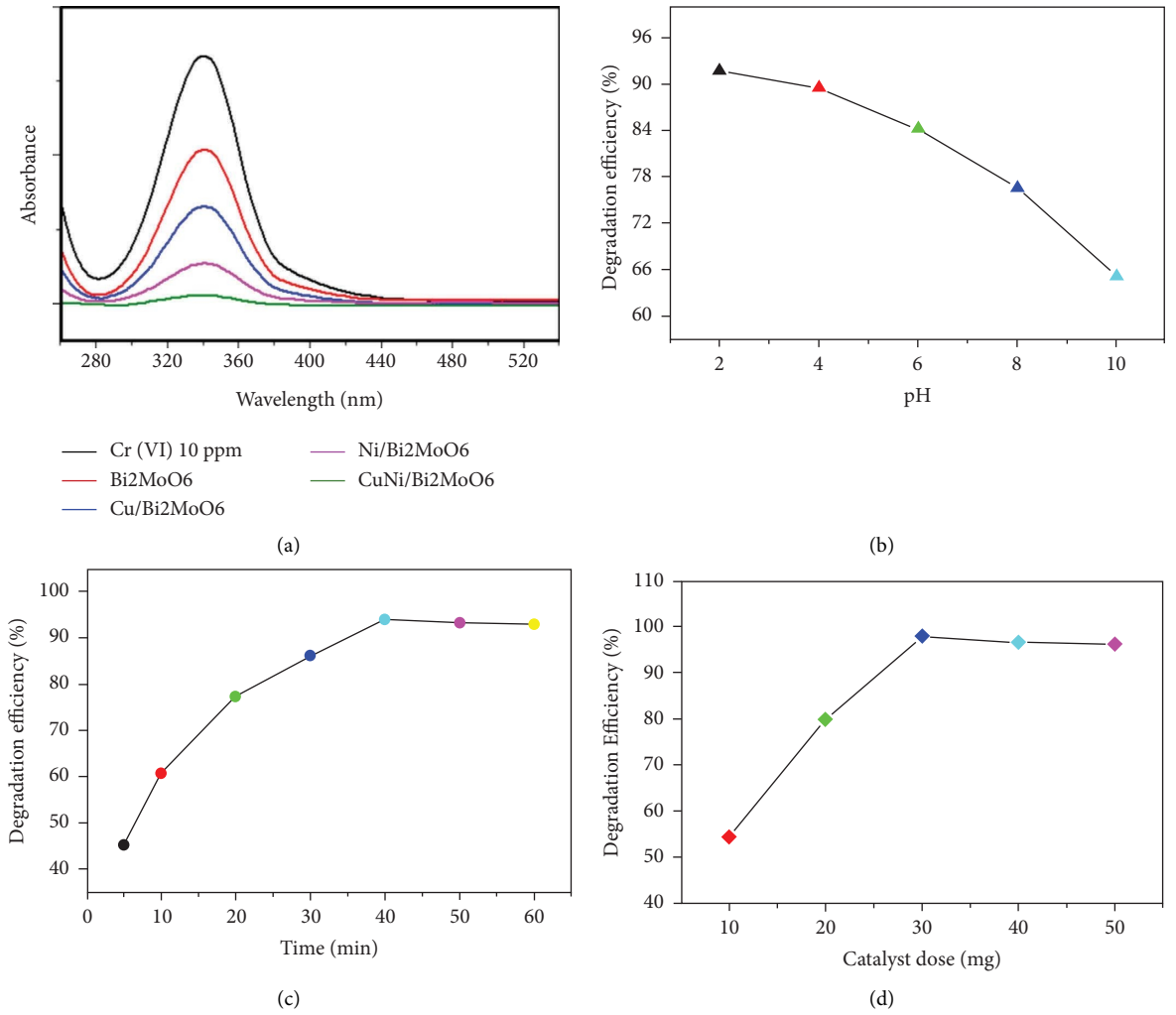

Figure 8: Continued.

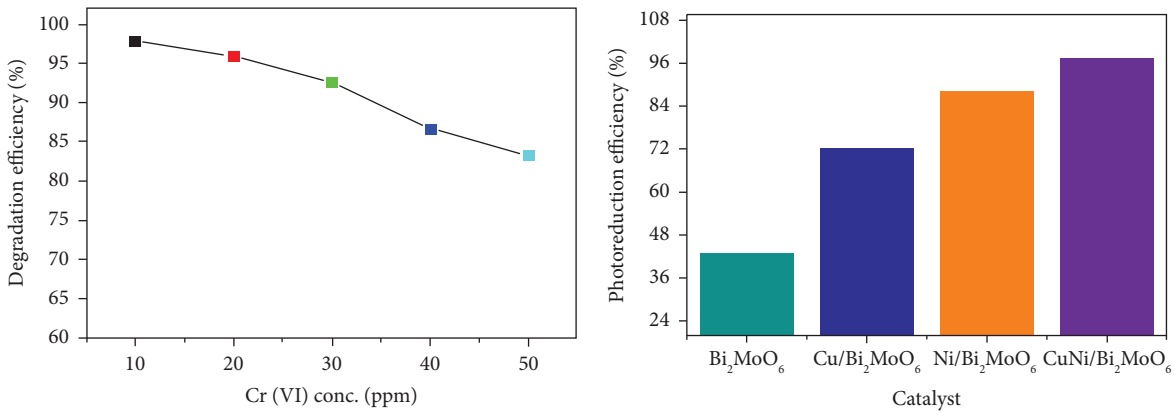

Figure 8: Optimization studies of Cr(VI) reduction: (a) UV-vis spectra for catalyst selection, (b) pH, (c) time, (d) catalyst dose, (e) $K_2Cr_2O_7$ concentration, and (f) percentage photoreduction efficiency comparison (pH: 4; time: 40 mins; catalyst does; 0.03 g; Cr(VI): 10 ppm).

a hinderance for the incident visible light and restrain it from striking the catalyst surface [28]. The other expected reason which justifies the drop in efficiency is the agglomeration of particles, which decreases the effective surface area of catalyst and decline in percentage degradation efficiency is anticipated [29].

3.6.6. Effect of $K_2Cr_2O_7$ Concentration on Cr(VI) Reduction. Effect of $K_2Cr_2O_7$ or Cr(VI) concentration on photoreduction efficiency was examined (at above optimized conditions) by varying its concentration from 10 ppm to 50 ppm. As shown in Figure 8(e), efficiency decreased with the increase in concentration. Photocatalytic efficiency was observed maximum at 10 ppm solution of $K_2Cr_2O_7$, so it was considered as optimum concentration. This trend can be explained by considering Beer–Lambert's law, when Cr(VI) concentration was increased it resulted in decrease of path length of photons entering the reaction vessel, as a result lesser photons were able to reach the catalyst surface. As the incident intensity, catalyst amount and irradiation time remained constant; therefore, the availability of active sites also reduced. After optimizing all the major factors are affecting photoreduction of hexavalent chromium; percentage photoreduction efficiencies of BMO, Cu/BMO, and Ni/BMO were also analysed at optimized conditions, and comparison is given in Figure 8(f).

In recent past, many photocatalysts have been utilized for the reduction of hexavalent chromium from waste water. Table 2 displays photoreduction of Cr(VI) by various photocatalysts. Comparative analysis shows that CuNi/Bi_2MoO_6 has better degradation ability than other reported catalysts.

3.7. Photodegradation Studies of Rhodamine B (RhB)

3.7.1. Selection of Appropriate Catalyst for RhB Degradation. Using UV-Visible absorption spectrophotometry, the photocatalytic efficiencies of four as fabricated catalysts (BMO, Cu/BMO, Ni/BMO, and CuNi/BMO) for the degradation of rhodamine B were inspected by taking 0.03 g of catalyst and 10 ppm RhB solution. The resulting solutions were irradiated under visible light for 40 minutes on continuous magnetic stirring. The most appropriate of these four catalysts was adopted based on its potency towards photodegradation. UV absorption values and color changes from intense pink to colorless solution showed that CuNi/BMO photocatalyst exhibited the highest photocatalytic activity among all photocatalysts as shown in Figure 9(a). Hence, CuNi/BMO was selected for further studies of rhodamine B degradation.

3.7.2. Effect of pH on Degradation of Rhodamine B. As different sources of wastewater possess different pH values, so pH has a straight influence on the surface charges of photocatalyst [39]. Effect of pH on degradation of RhB was studied in pH range 2–11 providing catalyst dose of 0.03 g in 40 mL of 10 ppm RhB solution for 30 minutes. Residual concentration of dye in the clear solution was determined with UV-Vis spectrophotometer. Catalytic efficiency of CuNi/Bi_2MoO_6 increases with the increase in pH (Figure 9(b)). Rhodamine B, being a cationic dye, would likely to develop electrostatic forces of attraction with the catalyst at pH above isoelectric point of BMO and its degradation will be enhanced. Maximum degradation efficiency was found at pH 10, so it was selected as optimum pH for further studies.

3.7.3. Effect of Irradiation Time on Degradation of Rhodamine B. Photodegradation of rhodamine B with the CuNi/Bi_2MoO_6 photocatalyst was studied at different time intervals from 5 to 40 minutes at pH 10 under visible light to optime the catalytic activity. The absorbance peak of RhB at maximum wavelength expeditiously declined with increase in exposure time accompanied by gradual decolorization of solution (Figure 9(c)). Electron transfer rate from valance band to conduction band increases, which is responsible for higher photocatalytic efficiency [40]. RhB was absolutely degraded after 30 minutes, so it was considered as optimum time. Figure 9(d) shows influence of time on percentage degradation efficiency of rhodamine B.

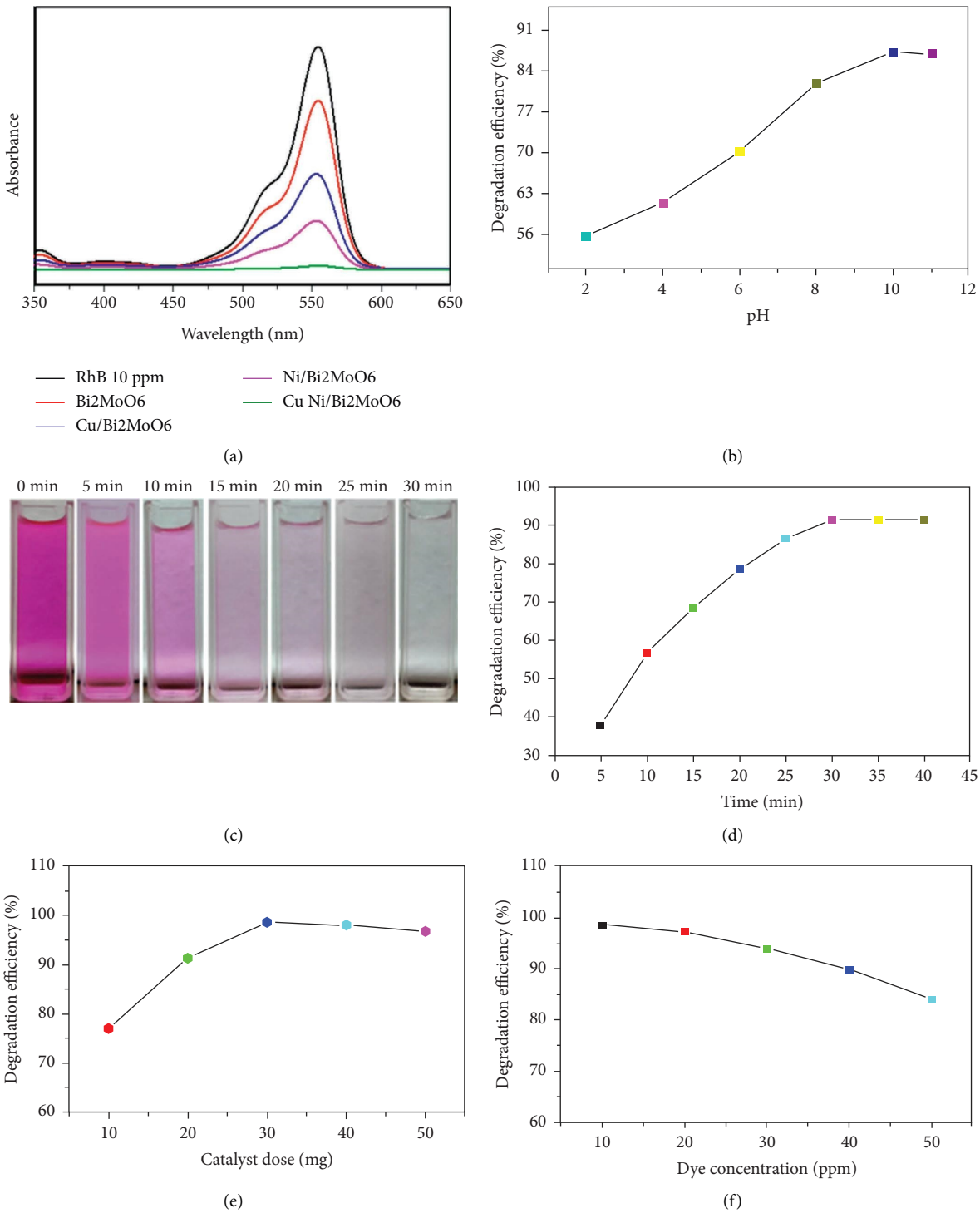

Figure 9: Continued.

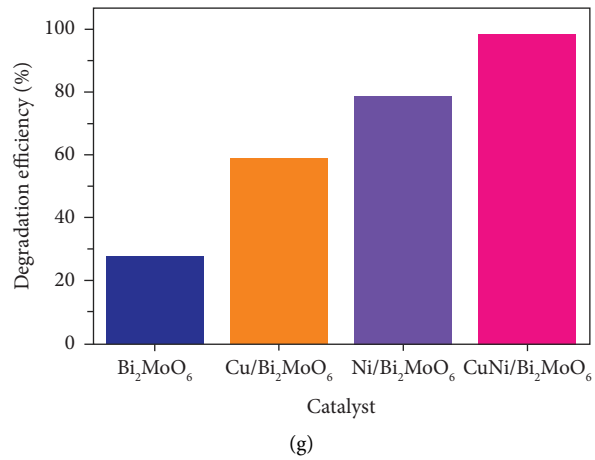

Figure 9: Photodegradation studies of RhB: (a) UV-Vis spectra for catalyst selection, (b) pH, (c) decolorization, (d) time, (e) catalyst dose, (f) RhB concentration, and (g) comparison for RhB degradation by various catalysts.

Table 2: Comparison of Cr(VI) photoreduction by various catalysts from the literature.

Catalysts	pH	Catalyst amount (g)	Cr(VI) (ppm)	Degradation time (min)	Degradation efficiency (%)	References
Au/N-TiO_2	—	1	10	240	90	[30]
Ag-Ag_2S/TiO_2	3	1	10	360	100	[31]
Bi_2O_3-TiO_2	3	1	20	180	73.9	[32]
g-C_3N_4	2	0.05	25	180	75	[33]
Chitosan/g-C_3N_4/TiO_2	2	0.33	30	240	90	[34]
Fe^{3+}-doped g-C_3N_4/MoS_2	—	0.03	20	120	91.4	[35]
Zn-MOF	—	0.04	10	90	93	[36]
Niobate/titanate	5	—	0.2	240	90	[37]
TiO_2/RGO/Fe_3O_4	4	0.56	—	100	95	[38]
CuNi/Bi_2MoO_6	4	0.03	10	40	97.92	This work
	4	0.03	50	40	85.1	

3.7.4. Effect of Catalyst Dose on Degradation of Rhodamine B. It is worth important to know about appropriate dosage of catalyst required for maximum efficiency not only for the estimation of cost but also for the recovery of photocatalyst after degradation process. It was studied by providing catalyst dose 0.01 g to 0.05 g at the above-given optimized conditions (Figure 9(e)). It is observed that the amount of CuNi/Bi_2MoO_6 in the solution has significantly influenced the efficiency of degradation process. Percentage degradation efficiency remarkably enhanced with the increase in catalyst amount as it was found to be maximum at 0.03 g of CuNi/Bi_2MoO_6. Catalytic efficiency declined with further increase in catalytic amount due to the reasons explained in Section 3.6.5.

3.7.5. Effect of Dye Concentration on Degradation of RhB. The degradation efficiency of RhB was examined by varying the concentration of RhB dye from 10 ppm to 50 ppm. Degradation efficiency of catalyst decreased with the increase in concentration of RhB as shown in Figure 9(f).

It may happen because adsorption of OH^- reduces due to increased adsorption of dye molecules on catalyst surface, and it causes a decrease in active sites of photocatalyst; as a result, the production of strongly oxidative $OH^\bullet$ radical is obstructed. Moreover, when the concentration of dye is high, it starts absorption of light to itself, hindering it to reach the catalyst surface [29]. Thus, less energy from photons hits the active sites of catalyst, resulting in lower amount of $OH^\bullet$ radicals. Furthermore, when the concentration of dye is high, then the formation of intermediate species may occur during the degradation process. These species may have potential to absorb those active radicals which react with dye molecules to degrade them. The overall efficiency decreases by increasing dye concentration due to these factors [41]. Figure 9(g) expresses the comparison percentage degradation efficiency of all the catalysts at optimized conditions. Different photocatalysts for RhB adsorption are listed in Table 3. These catalysts showed lower photocatalytic efficiency than our photocatalyst. CuNi/BMO photocatalyst showed the highest catalytic activity for the degradation of rhodamine B solution in just 30 minutes.

3.8. Photodegradation Studies of Malachite Green (MG)

3.8.1. Selection of the Appropriate Catalyst for MG Degradation. Using UV-Visible absorption spectrophotometry, the photocatalytic activities of four as synthesized catalysts for the degradation of malachite green were

Table 3: Comparison of RhB photodegradation by various catalysts from the previously reported literature.

Catalysts	Catalyst amount (mg)	Dye amount (ppm)	Degradation time (min)	Degradation efficiency (%)	References
Ag_3PO_4@GO	50	6	60	99	[42]
Ag_3PO_4/WO_3	40	5	30	97	[43]
Ag_3PO_4/Ag	100	10	90	98	[44]
Ag_3PO_4/ZnO	20	10	30	93	[45]
$LaNiO_3$	10	10	120	53	[46]
Ag_3PO_4/N-TiO_2	20	10	120	99	[47]
$Ag_3PO_4/BiVO_4$	100	10	30	92	[48]
Ag_2MoO_4/Ag_3PO_4	50	10	12	97	[49]
$AgBr/Ag_3PO_4$	100	10	7	99	[50]
$Bi_4Ti_3O_4/Ag_3PO_4$	20	5	30	99	[51]
g-C_3N_4/Ag_3PO_4	100	10	10	96	[52]
CNT/Ag_3PO_4	75	10	12	92.4	[53]
CuNi/Bi_2MoO_6	30	10	30	98.64	This work
	30	50	30	84.2	

examined by taking 0.02 g of each catalyst and 40 mL of 10 ppm malachite green solution. The solutions were irradiated under visible light for 40 minutes on continuous magnetic stirring. The most appropriate of these three catalysts was selected based on its efficiency towards degradation of dye. CuNi/Bi_2MoO_6 showed the maximum photodegradation efficiency for MG as compared to other three catalysts under same reaction conditions as shown in Figure 10(a). That is why the selected CuNi/BMO catalyst was used for further studies for MG degradation.

3.8.2. Effect of pH on Degradation of MG. Photodegradation of malachite green was analyzed at different values of pH ranging from 2 to 11, using 0.03 g catalyst in 10 ppm solution of MG for 30 minutes and maximum degradation was found at pH 10. Just like rhodamine B, MG is also a cationic dye so the optimization in basic media is justifiable due to the same reasons as explained in Section 3.7.2. PDE of CuNi/Bi_2MoO_6 for the removal of MG at pH values 2, 4, 6, 8, 10 and 11 is given in Figure 10(b).

3.8.3. Effect of Irradiation on Degradation of MG. In order to study the effect of time, a series of experiments was performed at different time intervals between 5 minutes to 40 minutes, providing 0.03 g catalyst in 10 ppm MG solution at pH 10. Catalytic efficiency increases by increasing the irradiation time as shown in Figure 10(c). It is may be due to the efficient electron transfer because electron transfer rate is upgraded by increasing the exposure time under visible light source [54]. MG was fully degraded after 20 minutes so, 20 minutes was selected as optimum time for further studies.

3.8.4. Effect of Catalyst Dose on Degradation of MG. Experimental studies were done to investigate the effect of photocatalyst amount on degradation of malachite green by varing the dose from 0.01 g to 0.05 g at above optimized conditions. Providing more catalyst dose raises the supply of active sites and more illuminated area for adsorption and photodegradation of dye molecules, thus the degradation rate increased upto certain amount of catalyst and then decreased [55]. Figure 10(e) shows that PDE of CuNi/Bi_2MoO_6 was found to be maximum at catalyst dosage of 0.02 g which depicts that it is a highly efficient photocatalyst for MG removal.

3.8.5. Effect of Dye Concentration on Degradation of MG. Effect of concentration of MG was studied in concentration range from 10 ppm to 50 ppm. Photodegradation of malachite green was found to be maximum in 10 ppm solution as shown in Figure 10(f). The possible reasons of high PDE at low dye concentration are explained in Section 3.7.5. After optimizing all the parameters, the photodegradation performances of BMO, Cu/BMO, and Ni/BMO were also studied. Figure 10(g) expresses the comparison percentage degradation efficiency of all the catalysts.

Comparision of photodegradation efficiency by various photocatalysts reported previously and superiority of CuNi/Bi_2MoO_6 synthesized in the current study is shown Table 4.

3.9. Effect of Adsorption on Photodegradation. Several experiments were conducted to better comprehend the relation between adsorption and photocatalysis. Comparative analyses on the dye degradation and Cr(VI) reduction caused by adsorption in the dark and photocatalysis under exposure to visible light were conducted. The adsorption of contaminants onto BMO surface without visible-light irradiation was examined for 40 minutes, nearly 20 to 25% contaminants adsorbed on catalyst surface. While they almost completely decomposed on photocatalysis under irradiation, revealing that the key factor in the complete dyes degradation was the photocatalysis.

3.10. Proposed Mechanism for Degradation of RhB and MG. It is believed that holes and superoxide anion radicals are responsible for the degradation of RhB and MG. When the light falls on the surface of the photocatalyst, holes and electrons are formed. Electrons react with the absorbed oxygen and form superoxide anionic radicals, whereas holes

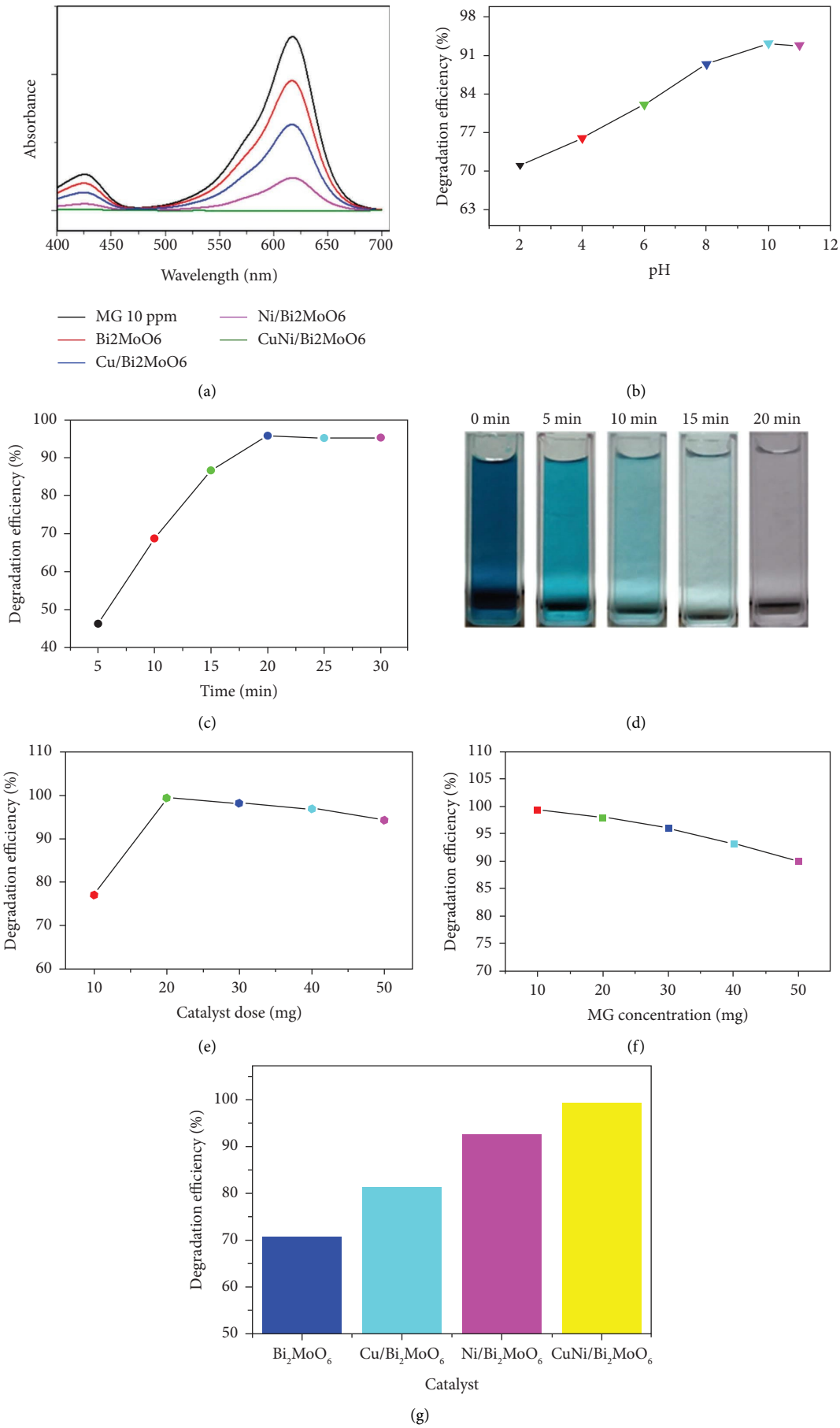

Figure 10: Photodegradation studies of RhB: (a) UV-Vis spectra for catalyst selection, (b) pH, (c) decolorization, (d) time, (e) catalyst dose, (f) MG concentration, and (g) comparison for MG degradation by various catalysts.

Table 4: Comparison of MG photodegradation by various catalysts from the literature.

Catalysts	Catalyst amount (g)	Dye amount (ppm)	Degradation time (min)	Degradation efficiency (%)	References
Sol-gel dip coating ZnO	—	5	180	69.53	[42]
MgFO/Ag0.69	1	3.6	150	70	[56]
TiO_2	0.25	10	60	78	[57]
$LiCoO_2$	0.5	18	20	73	[58]
c-ZnO NPs	0.24	20	60	90.20	[59]
Ag/g-C_3N_4	0.25	10	100	80	[60]
PANI/ZnO	0.4	3.6	300	89	[61]
Ce-SnO_2	10	10	120	92	[62]
CuNi/Bi_2MoO_6	0.02	10	20	99.42	This work
	0.02	50	20	89.5	

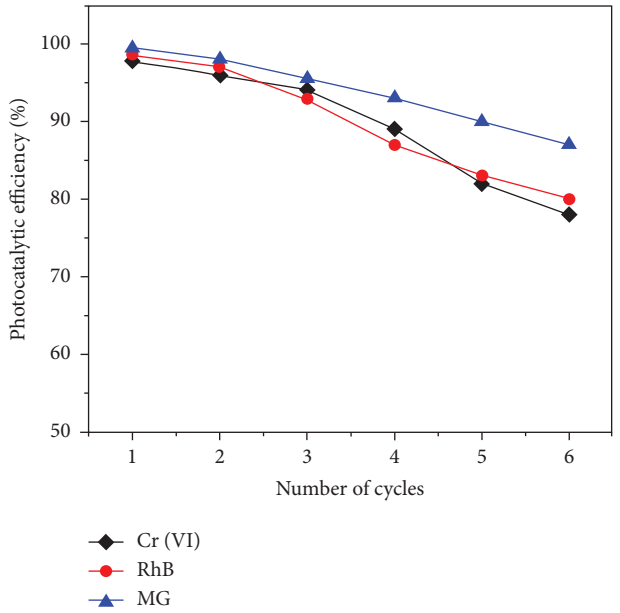

Figure 11: Reusability of the catalyst for photocatalytic efficiency.

react with the hydroxyl ions to form hydroxyl radicals. Since the electrons and hydroxyl radicals play a negligible role in the dye degradation, which is why only holes and superoxide anion radicals react with pollutants to degrade them into nontoxic products.

$$\begin{aligned} \mathbf{hv + Photocatalyst} &\longrightarrow \mathbf{h^+ + e^-} \\ \mathbf{O_2 + e^-} &\longrightarrow \mathbf{O_2^{\bullet -}} \\ \mathbf{OH^- + h^+} &\longrightarrow \mathbf{OH^{\bullet}} \\ \mathbf{Pollutant + h^+} &\longrightarrow \mathbf{Degradation\ products} \\ \mathbf{Pollutant + O_2^{\bullet -}} &\longrightarrow \mathbf{Degradation\ products} \end{aligned} \quad (9)$$

3.11. Reusability of the Catalyst. The fabricated Bi_2MoO_6 catalyst reusability was examined under optimized parameters for photocatalytic reactions (Figure 11). After the photodegradation process, the consumed Bi_2MoO_6 catalyst was recovered from the reaction products using centrifugation at 4000 rpm and washed with ethanol and water (3×), then dried in an oven at 100°C for 1 hour to eliminate any moisture or impurities before using it again for another cycle. For the first three cycles, the recycled catalyst exhibited negligible decrease in catalytic performance. However, the sixth cycle faced a reduction in catalytic performance to 80%. The similar trend was obtained for the removal efficiency of catalyst for of RhB and Cr(VI); however, the MG exhibits superior conversion efficiency even after the sixth cycle.

4. Conclusions

The bismuth molybdate photocatalyst was successfully doped and codoped with Ni^{2+} and Cu^{2+} ions by a facile hydrothermal method. All materials were characterized by XRD, Raman spectroscopy, and SEM which indicated orthorhombic geometry, phase purity, and increased surface roughness of modified materials. UV-visible spectrophotometry of modified materials shows strong photoabsorption in the visible region with band gap reduction. Transition metal doped and codoped Bi_2MoO_6 photocatalyst demonstrate extraordinarily improved photocatalytic performance for the removal of hexavalent chromium, rhodamine B, and malachite green from wastewater.

Photocatalytic efficiency of catalysts was found in the following order: $Ni/Bi_2MoO_6 > Ni/Bi_2MoO_6 > Cu/Bi_2MoO_6 > Bi_2MoO_6$. Doped and codoped materials exhibited amplification in photocatalytic performance which confirms low electron hole pair recombination and fast diffusion. Photocatalytic process was optimized by various parameters such as pH, time, catalyst dose, and concentration of contaminent. Under optimized conditions, $CuNi/Bi_2MoO_6$ exhibited 98.64% PDE in 30 minutes for RhB, 99.42% PDE in 20 minutes for MG, and 97.8% reduction efficiency in 40 minutes for Cr(VI). Using pseudofirst order reaction kinetics, values of rate constant for removal of RhB, MG, and Cr(VI) were found to be $0.1912\,min^{-1}$, $0.2378\,min^{-1}$, and $0.149\,min^{-1}$, respectively. Hence, it is concluded that Ni^{2+} and Cu^{2+} codoped Bi_2MoO_6 photocatalyst presents highest photocatalytic activity and can serve for the removal of hexavalent chromium, rhodamine B and malachite green from wastewater.

Data Availability

The original contributions presented in the study are included in the article/Supplementary Materials; further inquiries can be directed to the corresponding authors.

Conflicts of Interest

The authors declare that there are no potential conflicts of interest.

Acknowledgments

The authors are grateful to Pakistan Science Foundation for financial assistance under Project no. PSF-NSFC-IV/Chem/C-QAU (27).

Supplementary Materials

To assess the photocatalytic activity of the as prepared catalyst CuNi/BMO for colourless organic pollutants, bisphenol A was used before using with intensely coloured dyes (*Supplementary Materials*)

References

[1] S. Gita, A. Hussan, and T. Choudhury, "Impact of textile dyes waste on aquatic environments and its treatment," *Environment and Ecology*, vol. 35, pp. 2349–2353, 2017.

[2] S. Mondal, "Methods of dye removal from dye house effluent—an overview," *Environmental Engineering Science*, vol. 25, no. 3, pp. 383–396, 2008.

[3] Y. Deng and R. Zhao, "Advanced oxidation processes (AOPs) in wastewater treatment," *Current Pollution Reports*, vol. 1, no. 3, pp. 167–176, 2015.

[4] B. Szczepanik, "Photocatalytic degradation of organic contaminants over clay-T_iO2 nanocomposites: a review," *Applied Clay Science*, vol. 141, pp. 227–239, 2017.

[5] A. Areeb, T. Yousaf, M. Murtaza, M. Zahra, M. I. Zafar, and A. Waseem, "Green photocatalyst Cu/N_iO doped zirconia for the removal of environmental pollutants," *Materials Today Communications*, vol. 28, Article ID 102678, 2021.

[6] H. Li, W. Li, F. Wang, X. Liu, and C. Ren, "Fabrication of two lanthanides co-doped $B_i2M_oO_6$ photocatalyst: selection, design and mechanism of L_n1/L_n2 redox couple for enhancing photocatalytic activity," *Applied Catalysis B: Environmental*, vol. 217, pp. 378–387, 2017.

[7] Z. Dai, F. Qin, H. Zhao, J. Ding, Y. Liu, and R. Chen, "Crystal defect engineering of aurivillius $B_i2M_oO_6$ by Ce doping for increased reactive species production in photocatalysis," *ACS Catalysis*, vol. 6, no. 5, pp. 3180–3192, 2016.

[8] D. Kandi, S. Martha, A. Thirumurugan, and K. M. Parida, "CdS QDs-decorated self-dopedγ-$B_i2M_oO_6$: a sustainable and versatile photocatalyst toward photoreduction of Cr (VI) and degradation of phenol," *ACS Omega*, vol. 2, no. 12, pp. 9040–9056, 2017.

[9] D. Wang, H. Shen, L. Guo, C. Wang, and F. Fu, "Porous $B_iOB_r/B_i2M_oO_6$ heterostructures for highly selective adsorption of methylene blue," *ACS Omega*, vol. 1, no. 4, pp. 566–577, 2016.

[10] J. Wang, Y. Sun, C. Wu, Z. Cui, and P. Rao, "Enhancing photocatalytic activity of Bi2MoO6 via surface co-doping with N_i2^+ and T_i4^+ ions," *Journal of Physics and Chemistry of Solids*, vol. 129, pp. 209–216, 2019.

[11] X. Lin, X. Guo, D. Liu, Q. Wang, H. Zhai, and L. Chang, "S_iO^2/$Bi^2M_oO^6$ nanocomposites with high photocatalytic activity under visible light irradiation," *Materials Research Bulletin*, vol. 63, pp. 72–79, 2015.

[12] F. Huang, A. Yan, and H. Zhao, "Influences of doping on photocatalytic properties of Tio2 photocatalyst," *Semiconductor photocatalysis-materials, mechanisms and applications*, pp. 31–80, 2016.

[13] X. Zhang, X. Zhang, J. A. Johnson, Y. S. Chen, and J. Zhang, "Highly porous zirconium metal–organic frameworks with β-UH3-like topology based on elongated tetrahedral linkers," *Journal of the American Chemical Society*, vol. 138, no. 27, pp. 8380–8383, 2016.

[14] Y. Peng, Y. Zhang, F. Tian, J. Zhang, and J. Yu, "Structure tuning of $B_i2M_oO^6$ and their enhanced visible light photocatalytic performances," *Critical Reviews in Solid State and Materials Sciences*, vol. 42, no. 5, pp. 347–372, 2017.

[15] M. Wang, J. Han, P. Guo et al., "Hydrothermal synthesis of B-doped $B_i2M_oO^6$ and its high photocatalytic performance for the degradation of Rhodamine B," *Journal of Physics and Chemistry of Solids*, vol. 113, pp. 86–93, 2018.

[16] M. Wang, M. You, P. Guo et al., "Hydrothermal synthesis of Sm-doped $B_i2M_oO^6$ and its high photocatalytic performance for the degradation of Rhodamine B," *Journal of Alloys and Compounds*, vol. 728, pp. 739–746, 2017.

[17] X.-B. Zhang, L. Zhang, J.-S. Hu, and X. H. Huang, "Facile hydrothermal synthesis and improved photocatalytic activities of Z_n2^+ doped $B_i2M_oO^6$ nanosheets," *RSC Advances*, vol. 6, no. 38, pp. 32349–32357, 2016.

[18] L. Zhang, T. Xu, X. Zhao, and Y. Zhu, "Controllable synthesis of $B_i2M_oO^6$ and effect of morphology and variation in local structure on photocatalytic activities," *Applied Catalysis B: Environmental*, vol. 98, no. 3-4, pp. 138–146, 2010.

[19] W. Luo, J. Wang, X. Zhao, Z. Zhao, Z. Li, and Z. Zou, "Formation energy and photoelectrochemical properties of B_iVO^4 after doping at B_i3^+ or V^{5+} sites with higher valence metal ions," *Physical Chemistry Chemical Physics*, vol. 15, no. 3, pp. 1006–1013, 2013.

[20] X. Zhang, H. Zhang, H. Jiang, F. Yu, and Z. Shang, "Hydrothermal synthesis and characterization of C_e3^+ doped $B_i2M_oO^6$ for water treatment," *Catalysis Letters*, vol. 150, no. 1, pp. 159–169, 2020.

[21] Ö. Mergen and E. Arda, "Determination of optical band gap energies of CS/MWCNT Bio-nanocomposites by tauc and ASF methods," *Synthetic Metals*, vol. 269, Article ID 116539, 2020.

[22] M. Masnadi-Shirazi, R. Lewis, V. Bahrami-Yekta, T. Tiedje, M. Chicoine, and P. Servati, "Bandgap and optical absorption edge of $G_aAs_{1-x}Bi_x$ alloys with $0< x< 17.8\%$," *Journal of Applied Physics*, vol. 116, no. 22, Article ID 223506, 2014.

[23] B. Hameeda, A. Mushtaq, M. Saeed, A. Munir, U. Jabeen, and A. Waseem, "Development of Cu-doped N_iO nanoscale material as efficient photocatalyst for visible light dye degradation," *Toxin Reviews*, vol. 40, no. 4, pp. 1396–1406, 2021.

[24] T. Chankhanittha and S. Nanan, "Visible-light-driven photocatalytic degradation of ofloxacin (OFL) antibiotic and Rhodamine B (RhB) dye by solvothermally grown Z_nO/$B_i2M_oO^6$ heterojunction," *Journal of Colloid and Interface Science*, vol. 582, pp. 412–427, 2021.

[25] T. B. Iorhuna, A. R. Wuana, and G. S. Yiase, "Effect of dissolved organic matter, DOM on the kinetics of simultaneous studies of oxidation of arsenic (III) and reduction of chromium (VI) in aqueous phase," *IOSR Journal of Applied Chemistry*, vol. 13, pp. 54–66, 2020.

[26] E. Wahyuni, N. Aprilita, H. Hatimah, A. Wulandari, and M. Mudasir, "Removal of toxic metal ions in water by photocatalytic method," *American Chemical Science Journal*, vol. 5, no. 2, pp. 194–201, 2015.

[27] H. Li, J. Li, P. Yang, D. H. Ng, X. Cui, and F. Ji, "Three-dimensional biogenic C-doped $B_i2M_oO_6$/In^2O^3-Z_nOZ-scheme heterojunctions derived from a layered precursor," *Journal of Environmental Sciences*, vol. 79, pp. 54–66, 2019.

[28] V. Etacheri, C. Di Valentin, J. Schneider, D. Bahnemann, and S. C. Pillai, "Visible-light activation of T_iO^2 photocatalysts: advances in theory and experiments," *Journal of Photochemistry and Photobiology C: Photochemistry Reviews*, vol. 25, pp. 1–29, 2015.

[29] Z. Vasiljevic, M. Dojcinovic, and J. Vujancevic, "Photocatalytic degradation of methylene blue under natural sunlight using iron titanate nanoparticles prepared by a modified sol–gel method," *Royal Society open science*, vol. 7, Article ID 200708, 2020.

[30] X. Liu, L. Pan, T. Lv, Z. Sun, and C. Sun, "Sol–gel synthesis of A_u/N–T_iO^2 composite for photocatalytic reduction of Cr (vi)," *RSC Advances*, vol. 2, no. 9, pp. 3823–3827, 2012.

[31] D. Zhang, G. Xu, and F. Chen, "Hollow spheric Ag–A_g2S/T_iO2 composite and its application for photocatalytic reduction of Cr (VI)," *Applied Surface Science*, vol. 351, pp. 962–968, 2015.

[32] J. Yang, J. Dai, and J. Li, "Visible-light-induced photocatalytic reduction of Cr (VI) with coupled B_i2O^3/T_iO^2 photocatalyst and the synergistic bisphenol A oxidation," *Environmental Science and Pollution Research*, vol. 20, no. 4, pp. 2435–2447, 2013.

[33] X. Wang, Z. Zhou, Z. Liang, Z. Zhuang, and Y. Yu, "Photochemical synthesis of the Fe0/C_3N_4/MoS2 heterostructure as a highly active and reusable photocatalyst," *Applied Surface Science*, vol. 423, pp. 225–235, 2017.

[34] Q.-H. Li, M. Dong, R. Li et al., "Enhancement of Cr (VI) removal efficiency via adsorption/photocatalysis synergy using electrospun chitosan/g-C_3N_4/T_iO2 nanofibers," *Carbohydrate Polymers*, vol. 253, Article ID 117200, 2021.

[35] X. Wang, M. Hong, F. Zhang, Z. Zhuang, and Y. Yu, "Recyclable nanoscale zero valent iron doped g-C_3N_4/MoS^2 for efficient photocatalysis of RhB and Cr (VI) driven by visible light," *ACS Sustainable Chemistry & Engineering*, vol. 4, no. 7, pp. 4055–4063, 2016.

[36] H. Kaur, S. Sinha, V. Krishnan, and R. R. Koner, "Photocatalytic reduction and recognition of Cr (VI): new Zn (II)-based metal– organic framework as catalytic surface," *Industrial & Engineering Chemistry Research*, vol. 59, no. 18, pp. 8538–8550, 2020.

[37] X. Liu, P. Du, W. Pan et al., "Immobilization of uranium (VI) by niobate/titanate nanoflakes heterojunction through combined adsorption and solar-light-driven photocatalytic reduction," *Applied Catalysis B: Environmental*, vol. 231, pp. 11–22, 2018.

[38] Z.-J. Li, Z.-W. Huang, W.-L. Guo et al., "Enhanced photocatalytic removal of uranium (VI) from aqueous solution by magnetic T_iO^2/F_e3O^4 and its graphene composite," *Environmental Science & Technology*, vol. 51, no. 10, pp. 5666–5674, 2017.

[39] A. Alkaim, A. Aljeboree, N. Alrazaq, S. Baqir, F. Hussein, and A. Lilo, "Effect of pH on adsorption and photocatalytic degradation efficiency of different catalysts on removal of methylene blue," *Asian Journal of Chemistry*, vol. 26, no. 24, pp. 8445–8448, 2014.

[40] M. Abdellah, S. Nosier, A. El-Shazly, and A. Mubarak, "Photocatalytic decolorization of methylene blue using T_iO2/UV system enhanced by air sparging," *Alexandria Engineering Journal*, vol. 57, no. 4, pp. 3727–3735, 2018.

[41] S. Balu, K. Uma, G.-T. Pan, T. Yang, and S. Ramaraj, "Degradation of methylene blue dye in the presence of visible light using S_iO2@α-F_e2O3 nanocomposites deposited on SnS2 flowers," *Materials*, vol. 11, no. 6, p. 1030, 2018.

[42] R. Liu, H. Li, L. Duan, H. Shen, Q. Zhang, and X. Zhao, "The synergistic effect of graphene oxide and silver vacancy in A_g3PO^4-based photocatalysts for rhodamine B degradation under visible light," *Applied Surface Science*, vol. 462, pp. 263–269, 2018.

[43] J. Zhang, K. Yu, Y. Yu et al., "Highly effective and stable A_g3PO^4/WO^3 photocatalysts for visible light degradation of organic dyes," *Journal of Molecular Catalysis A: Chemical*, vol. 391, pp. 12–18, 2014.

[44] K. Huang, Y. Lv, W. Zhang et al., "One-step synthesis of Ag 3 PO 4/Ag photocatalyst with visible-light photocatalytic activity," *Materials Research*, vol. 18, no. 5, pp. 939–945, 2015.

[45] C. Dong, K.-L. Wu, M.-R. Li, L. Liu, and X. W. Wei, "Synthesis of A_g3PO^4–Z_nO nanorod composites with high visible-light photocatalytic activity," *Catalysis Communications*, vol. 46, pp. 32–35, 2014.

[46] A. Ghafoor, I. Bibi, S. Ata et al., "Energy band gap tuning of L_aNiO^3 by Gd, Fe and Co ions doping to enhance solar light absorption for efficient photocatalytic degradation of RhB dye: a mechanistic approach," *Journal of Molecular Liquids*, vol. 343, Article ID 117581, 2021.

[47] N. Khalid, U. Mazia, M. Tahir, N. Niaz, and M. A. Javid, "Photocatalytic degradation of RhB from an aqueous solution using A_g3PO^4/N- T_iO2 heterostructure," *Journal of Molecular Liquids*, vol. 313, Article ID 113522, 2020.

[48] X. Qi, M. Gu, X. Zhu et al., "Controlled synthesis of A_g3PO^4/B_iVO^4 composites with enhanced visible-light photocatalytic performance for the degradation of RhB and 2, 4-DCP," *Materials Research Bulletin*, vol. 80, pp. 215–222, 2016.

[49] W. Cao, Y. An, L. Chen, and Z. Qi, "Visible-light-driven A_g2MoO^4/A_g3PO^4 composites with enhanced photocatalytic activity," *Journal of Alloys and Compounds*, vol. 701, pp. 350–357, 2017.

[50] B. Wang, X. Gu, Y. Zhao, and Y. Qiang, "A comparable study on the photocatalytic activities of A_g3PO^4, A_gBr and AgBr/Ag^3PO^4 hybrid microstructures," *Applied Surface Science*, vol. 283, pp. 396–401, 2013.

[51] C. Zheng, H. Yang, Z. Cui, H. Zhang, and X. Wang, "A novel B_i4T_i3O12/Ag^3PO^4 heterojunction photocatalyst with enhanced photocatalytic performance," *Nanoscale Research Letters*, vol. 12, pp. 608–612, 2017.

[52] P. He, L. Song, S. Zhang, X. Wu, and Q. Wei, "Synthesis of g-C_3N_4/Ag3PO^4 heterojunction with enhanced photocatalytic performance," *Materials Research Bulletin*, vol. 51, pp. 432–437, 2014.

[53] H. Xu, C. Wang, Y. Song et al., "CNT/Ag3PO^4 composites with highly enhanced visible light photocatalytic activity and stability," *Chemical Engineering Journal*, vol. 241, pp. 35–42, 2014.

[54] M. Flores-Flores, E. Luévano-Hipólito, L. M. T. Martínez, G. Morales-Mendoza, and R. Gómez, "Photocatalytic CO2 conversion by MgAl layered double hydroxides: effect of Mg2+ precursor and microwave irradiation time," *Journal of Photochemistry and Photobiology A: Chemistry*, vol. 363, pp. 68–73, 2018.

[55] W. Szeto, C. W. Kan, C. Yuen, S. W. Chan, and K. H. Lam, "Effective photodegradation of methyl orange using fluidized bed reactor loaded with cross-linked chitosan embedded nano-CdS photocatalyst," *International Journal of Chemical Engineering*, vol. 2014, Article ID 270946, 16 pages, 2014.

[56] M. Tsvetkov, J. Zaharieva, and M. Milanova, "Ferrites, modified with silver nanoparticles, for photocatalytic degradation of malachite green in aqueous solutions," *Catalysis Today*, vol. 357, pp. 453–459, 2020.

[57] T. Sreekanth, J.-J. Shim, and Y. R. Lee, "Degradation of organic pollutants by bio-inspired rectangular and hexagonal titanium dioxide nanostructures," *Journal of Photochemistry and Photobiology B: Biology*, vol. 169, pp. 90–95, 2017.

[58] C. R. Michel, M. A. Lopez-Alvarez, and A. H. Martínez-Preciado, "Novel UV sensing and photocatalytic properties of nanostructured LiCoO2 prepared by the coprecipitation method," *Journal of Photochemistry and Photobiology A: Chemistry*, vol. 403, Article ID 112842, 2020.

[59] M. A. Kumar, C. Ravikumar, H. Nagaswarupa et al., "Evaluation of bi-functional applications of ZnO nanoparticles prepared by green and chemical methods," *Journal of Environmental Chemical Engineering*, vol. 7, no. 6, Article ID 103468, 2019.

[60] P. C. Nagajyothi, M. Pandurangan, S. Vattikuti, C. Tettey, T. Sreekanth, and J. Shim, "Enhanced photocatalytic activity of Ag/g-C3N4 composite," *Separation and Purification Technology*, vol. 188, pp. 228–237, 2017.

[61] V. Eskizeybek, F. Sarı, H. Gülce, A. Gülce, and A. Avcı, "Preparation of the new polyaniline/ZnO nanocomposite and its photocatalytic activity for degradation of methylene blue and malachite green dyes under UV and natural sun lights irradiations," *Applied Catalysis B: Environmental*, vol. 119-120, pp. 197–206, 2012.

[62] N. Chen, B. Liu, P. Zhang et al., "Enhanced photocatalytic performance of Ce-doped SnO2 hollow spheres by a one-pot hydrothermal method," *Inorganic Chemistry Communications*, vol. 132, Article ID 108848, 2021.